RSC Advances

PAPER

View Article Online
View Journal | View Issue

Cite this: *RSC Adv.*, 2025, **15**, 50111

Sustainable co-production of carbon quantum dots and activated carbon from natural rubber latex for the inhibition of pathogenic microorganisms and removal of pharmaceutical residues

Satit Yousatit,[ab] Sakdinun Nuntang,[c] Toshiyuki Yokoi,[d] Chawalit Ngamcharussrivichai*[ab] and Napida Hinchiranan *[ab]

This study demonstrates a sustainable and integrated method for the co-production of carbon quantum dots (CQDs) and activated carbon (AC) using natural rubber (NR) latex, which is a renewable and widely available biomass. CQDs were synthesized *via* a hydrothermal method using cetyltrimethylammonium bromide and nitric acid as nitrogen dopants. The as-formed product comprised uniform amorphous nanoparticles (3.5–11.0 nm) that exhibited intense blue photoluminescence and abundant surface amino and oxygen-containing groups. The CQDs exhibited excellent antimicrobial and antiviral activities, achieving >99.9% inactivation of *Staphylococcus aureus*, *Micrococcus luteus*, *Escherichia coli*, *Candida albicans*, *Aspergillus niger*, and influenza A virus (H3N2) within 5 min of exposure at a concentration of 15 μg mL^{-1}. Moreover, they demonstrated negligible cytotoxicity toward HaCaT keratinocytes. Furthermore, the hydrochar obtained as a by-product of hydrothermal synthesis was subsequently converted into AC *via* physical and chemical activation, yielding a large-surface-area adsorbent (up to 1167 m^2 g^{-1}) featuring a diclofenac uptake capacity of 126.82 mg g^{-1} at 25 °C. The adsorption process followed pseudo-second-order kinetics and a Langmuir-type monolayer adsorption mechanism. Adsorption mainly proceeded *via* π–π interactions, hydrogen bonding, and electrostatic attraction between diclofenac molecules and heteroatom-rich surface sites. This dual-function valorization of NR latex simultaneously addresses microbial and pharmaceutical pollution, advancing circular bioeconomy principles and offering sustainable solutions for water treatment and healthcare applications.

Received 9th October 2025
Accepted 8th December 2025

DOI: 10.1039/d5ra07708g

rsc.li/rsc-advances

1. Introduction

Water scarcity has emerged as a critical global concern, as the demand for freshwater has already exceeded the available supply in numerous regions.[1] Consequently, the reuse of treated wastewater is gaining increasing attention as an essential strategy for establishing safe and sustainable water resources. This strategic imperative is reflected in International, European, and National Water Management policies and directly aligns with the objectives of Sustainable Development Goal 6 stipulated by United Nations, aiming to substantially increase global water recycling and safe reuse by 2030.[2,3] Disinfection is a crucial step in conventional water and wastewater treatment and is typically conducted using oxidizing agents, such as chlorine or ozone, to inactivate pathogenic microorganisms.[4] However, these disinfectants readily react with pharmaceutical residues in wastewater, generating disinfection by-products (DBPs), such as trihalomethanes and haloacetic acids. These compounds exhibit cytotoxicity, genotoxicity, and potential carcinogenicity.[5] Moreover, the persistence of DBPs in aquatic environments renders their removal *via* conventional treatment methods difficult,[6] raising concerns regarding their environmental persistence and human health risks. To advance safe and sustainable water reuse, the development of innovative treatment technologies that can simultaneously address microbial and pharmaceutical contamination as well as prevent DBP formation is essential.

Carbon quantum dots (CQDs), which are a class of zero-dimensional carbon nanomaterials featuring the diameters of <10 nm, have emerged as promising antimicrobial agents owing to their facile surface functionalization, cost-effectiveness, and excellent biocompatibility.[7] Various strategies have been developed for CQD synthesis, and they are generally classified as top-

[a]*Department of Chemical Technology, Faculty of Science, Chulalongkorn University, Pathumwan, Bangkok 10330, Thailand. E-mail: Napida.H@chula.ac.th; Chawalit.Ng@chula.ac.th*

[b]*Center of Excellence in Catalysis for Bioenergy and Renewable Chemicals (CBRC), Faculty of Science, Chulalongkorn University, Pathumwan, Bangkok 10330, Thailand*

[c]*Industrial Chemistry Innovation Program, Faculty of Science, Maejo University, Chiang Mai 50290, Thailand*

[d]*Nanospace Catalysis Research Unit, Institute of Integrated Research, Institute of Science Tokyo, 4259 Nagatsuta, Midori-ku, Yokohama 226-8503, Japan*

down and bottom-up approaches. Top-down methods rely on the fragmentation of large sp^2 carbon structures, such as graphite[8] and carbon fibers,[9] into nanoscale fragments. Although these methods offer high product yields, they commonly require harsh conditions and expensive instrumentation.[10] Furthermore, these methods offer limited control over the particle size, morphology, and surface chemistry.[11] Conversely, bottom-up methods involve the assembly of small organic molecules or oligomers into sp^2 carbon domains.[12,13] Among them, hydrothermal synthesis has garnered particular attention because of its cost-effectiveness, eco-friendliness, and ability to produce CQDs featuring uniform size distribution, tunable surface functionalities, and high quantum yields.[14] Natural rubber (NR), which is a renewable biopolymer primarily produced in Southeast Asia, is predominantly composed of *cis*-1,4-polyisoprene.[15] Its conjugated double bonds provide a reactive structural framework suitable for carbonization.[16] Despite its abundance, high carbon content, and intrinsic sustainability, NR has been rarely explored as a precursor in CQD synthesis. NR latex used in this study is a cost-effective, renewable feedstock abundantly available in Thailand. Moreover, the valorization of NR into high-value carbon nanomaterials offers a promising opportunity to broaden the application scope of NR and enhance its economic value. This is particularly relevant because of its surplus production in Thailand and price volatility in the rubber market. Furthermore, this strategy does not compete with existing rubber applications, such as tire and glove production, but rather supports the national Bio-Circular-Green economy initiative by creating sustainable downstream uses for agricultural products.

The antimicrobial activity of CQDs is considerably affected by their particle size and surface charge, which can be tuned by modulating synthesis conditions and surface functionalization.[17] The underlying mechanisms of the antimicrobial activity of CQDs include the direct disruption of microbial membranes and the generation of reactive oxygen species (ROS), leading to cell death.[18] Recently, porous, nitrogen-doped carbon nanosheets featuring high content of graphitic nitrogen and abundant defect sites have been demonstrated to possess enhanced oxygen reduction activity, indicating the effects of nitrogen functionalities and carbon microstructures on interfacial electron transfer and adsorption behavior.[19] Insights derived from the study of electroactive carbons are highly relevant for the design of nitrogen-doped CQDs, in which graphitic and pyridinic/pyrrolic N species can simultaneously modulate redox activity, surface charge, and affinity toward microbial membranes.[20] Nitrogen-doped CQDs demonstrate high activity against both Gram-negative *Escherichia coli* (*E. coli*) and Gram-positive *Bacillus subtilis* (*B. subtilis*), which is attributed to strong electrostatic interactions between negatively charged bacterial membranes and the protonated nitrogen functionalities of CQDs.[21] Similarly, CQDs possessing quaternary ammonium groups display potent antibacterial effects against Gram-positive *Staphylococcus aureus* (*S. aureus*) and Gram-negative *E. coli* because of synergistic electrostatic and hydrophobic interactions.[22,23] Additionally, oxygen-rich CQDs derived from renewable precursors, such as guar gum[24] and vitamin C,[25] have demonstrated antifungal activity against *Rhizoctonia solani*, *Pyricularia grisea*, and *Candida albicans* (*C. albicans*). Moreover, CQDs are gaining increasing attention owing to their antiviral potential. They can inhibit a wide array of viruses, including Japanese encephalitis virus, Zika virus, dengue virus, herpes simplex virus, and coronaviruses, by blocking viral attachment, penetration, replication, or budding.[17,26] Collectively, these findings emphasize CQDs as a versatile platform featuring broad-spectrum antimicrobial and antiviral properties, offering innovative opportunities for the sustainable management and control of emerging infectious diseases.

Adsorption is a promising technique for the removal of pharmaceutical contaminants from water, offering simple operation, cost-effectiveness, and high efficiency.[27] In particular, carbon-based adsorbents are versatile materials because their performance can be modulated by adjusting their pore structure and surface functionalities. Among the available adsorbents, activated carbon (AC) has gained attention because of its large surface area, porous architecture, surface functionalities, and hydrophobicity, which collectively enable the capture of diverse organic pollutants.[28] In addition to conventional AC, biochar-derived adsorbents produced using unconventional feedstocks, such as municipal sludge and peat, demonstrate high adsorption capacities after chemical activation, indicating that feedstock selection and activation conditions critically affect the structural development and performance of adsorbents.[29] However, biochars may exhibit variability in quality, pore structure, and residual inorganic content, which can adversely affect the consistency of activation and performance in large-scale applications. Recently, hydrochar obtained as a by-product of the hydrothermal process has gained attention as a promising precursor for AC production. Its carbon-rich structure and broad availability enable its effective transformation into high-performance AC *via* physical or chemical activation,[30] contributing to improved resource utilization and reduced waste generation. This valorization pathway that converts residues into functional carbon materials for environmental remediation is consistent with the circular economy principles.

In this study, we develop a sustainable one-pot strategy for the conversion of NR latex into two functional carbon materials, namely, nitrogen-doped CQDs that exhibit rapid, broad-spectrum antimicrobial activity and porous AC capable of pharmaceutical adsorption. By integrating the formation of these complementary materials within a single synthesis pathway, this study establishes an efficient and zero-waste approach for the generation of multifunctional carbon materials for water purification and health-related applications.

2. Materials and methods

2.1 Preparation of the CQD solution

The CQDs were synthesized using NR latex (60%; Rubber Division, Department of Agriculture, Ministry of Agriculture and Cooperatives, Thailand) *via* a hydrothermal method. Cetyltrimethylammonium bromide (CTAB; 99%; AR grade; Loba, India) and nitric acid (65%; AR grade; QRëC, New Zealand) were used

as nitrogen sources. A schematic of the synthesis procedures for the CQDs and hydrochar is illustrated in Fig. 1. First, 0.9 g of CTAB was dissolved in 26.6 mL of deionized water, and NR latex (2 g) was subsequently added. The mixture was stirred for 30 min, and 10.5 g of a nitric acid solution was added dropwise under continuous stirring. The resulting suspension was transferred to a Teflon-lined stainless-steel autoclave and subjected to hydrothermal treatment at 170 °C for 24 h. After cooling, the product was separated into liquid and solid *via* filtration. The liquid fraction was centrifuged at 6000 rpm for 15 min to remove residual precipitates, and the supernatant was further purified using a 200 nm syringe filter (Filtrex, Thailand). The resulting dark brown aqueous solution containing the CQDs was collected and stored for subsequent characterization and antimicrobial/adsorption studies. The solid hydrochar by-product was retained and used as the precursor for AC production.

2.2 Preparation of AC

AC was synthesized using the hydrochar residue generated during CQD synthesis *via* chemical or thermal activation. For chemical activation, 1 g of hydrochar was mixed with 2 g of a 25 wt% KOH (≥85%; AR grade; VWR Chemicals, England) solution. Thereafter, the mixture was thermally treated in a tube furnace under an Ar flow (80 mL min^{-1}) by heating at a heating rate of 10 °C min^{-1} to 600 °C, followed by a holding period of 3 h at this temperature. The resulting carbon material was repeatedly washed with 3 M HCl (37%; AR grade; Merck, Germany) and deionized water until neutral pH was reached, followed by drying at 110 °C overnight. The as-obtained sample was labeled CAC. For thermal activation, hydrochar was directly pyrolyzed at 900 °C for 3 h under an Ar flow of 80 mL min^{-1}, without any chemical addition. The resulting product was labeled TAC.

2.3 Characterization of materials

The physicochemical properties of the CQDs, hydrochar, and AC were characterized using various techniques. Structural features were examined *via* powder X-ray diffraction (XRD), and particle size distribution was determined using dynamic light scattering (DLS). Morphological characteristics were explored *via* transmission electron microscopy (TEM). Textural properties, including surface area and porosity, were determined *via* nitrogen physisorption analysis. Surface functionalities were probed using Fourier transform infrared (FTIR) spectroscopy and X-ray photoelectron spectroscopy (XPS). Optical properties were evaluated using ultraviolet-visible (UV-vis) absorption and fluorescence spectroscopy. Detailed descriptions of the instruments and their operating conditions are provided in the SI.

2.4 Antimicrobial and antiviral activity

The antimicrobial activity of the CQDs was assessed against Gram-positive bacteria (*S. aureus*, *Micrococcus luteus* (*M. luteus*), and *B. subtilis*), Gram-negative bacteria (*E. coli* and *Klebsiella pneumoniae* (*K. pneumoniae*)), and fungi (*C. albicans* and *Aspergillus niger* (*A. niger*)). All microbial strains used in this study were obtained from the Thailand Institute of Scientific and Technological Research (TISTR), Thailand. Antimicrobial susceptibility was first evaluated using the disk diffusion method by measuring inhibition zones. The minimum inhibitory concentration (MIC) and minimum bactericidal concentration (MBC) were determined *via* the broth microdilution method. Additionally, time-kill assays and quantitative microbial tests were conducted using the broth macrodilution method following ASTM E2149-10 with minor modifications. The antiviral activity of the CQDs was tested against influenza A virus (H3N2) in Madin–Darby Canine Kidney (MDCK) cells using the virus inhibition assay and 50% tissue culture infectious dose assay in accordance with ASTM E1053-20.[31] The

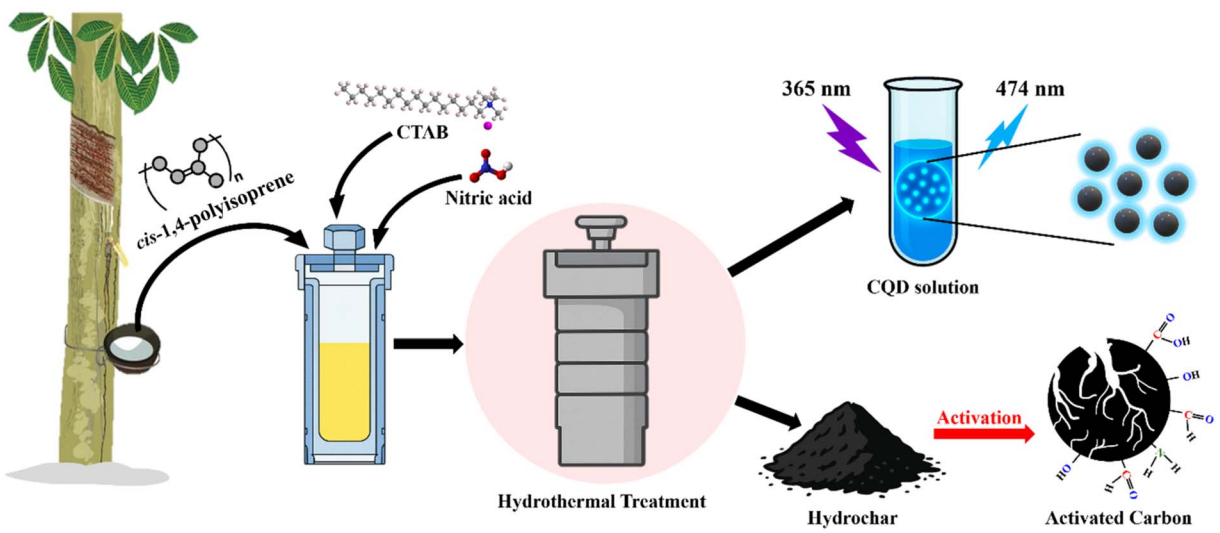

Fig. 1 Schematic of the sustainable co-production of the CQDs and AC using NR latex *via* the hydrothermal method.

influenza A virus (H3N2) strain was obtained from the Department of Medical Sciences of the Ministry of Public Health (Thailand) and the MDCK cells were purchased from the American Type Culture Collection (ATCC, USA). Detailed protocols and assay conditions for both antimicrobial and antiviral evaluations are provided in the SI.

2.5 Cytotoxicity study

The cytotoxicity of the CQD solution was evaluated using the 3-[4,5-dimethylthiazol-2-yl]-2,5 diphenyl tetrazolium bromide (MTT) assay. Human keratinocyte (HaCaT) cells were purchased from American Type Culture Collection (ATCC, USA). HaCaT cells were cultured and seeded into 96-well plates at a density of 6×10^3 cells per well, followed by overnight incubation. Thereafter, the cells were exposed to the CQD solutions at the concentrations of 0.042–140 μg mL^{-1} for 24 h. Subsequently, 10 μL of the MTT solution (5 mg mL^{-1}) was added to each well, followed by incubation at 37 °C in a 5% CO_2 atmosphere for 4 h. The resulting formazan crystals were dissolved in 100 μL of the solubilization solution, and absorbance was measured at 570 nm using a microplate reader. Dimethyl sulfoxide was employed as the vehicle control. Cell viability was expressed as a percentage relative to that of control.

2.6 Adsorption experiments

The adsorption performance of hydrochar and AC toward diclofenac sodium (DCF; 98%; HPLC grade; TCI, Japan) was evaluated *via* batch equilibrium sorption experiments. DCF solutions featuring concentrations in the range of 10–50 mg L^{-1} were prepared *via* the serial dilution of a 100 mg L^{-1} stock solution in deionized water. Prior to use, adsorbents were oven-dried at 100 °C overnight. In a typical run, 45 mg of adsorbent was added to 150 mL of the DCF solution and agitated in a thermostat-controlled shaking water bath (125 rpm; 25 °C) until equilibrium was reached. Thereafter, the suspensions were filtered using a 0.22 μm hydrophobic polytetrafluoroethylene syringe filter, and the residual DCF concentration was quantified *via* UV-vis spectrophotometry at 276 nm (V-530, Jasco, Japan). All adsorption experiments were performed in triplicate, and average values were reported. Adsorption kinetics were modeled using pseudo-first-order and pseudo-second-order equations, and equilibrium data were analyzed utilizing Langmuir and Freundlich isotherms. Details of the calculation procedures and model fitting methods are provided in the SI.

3. Results and discussion

3.1 Characterization of the CQDs

The structural properties of the CQDs were first examined *via* XRD (Fig. 2A). The board diffraction peak centered at $2\theta \approx 21.5°$ corresponded to the (002) plane of the amorphous structure of the CQDs (JCPDS card no. 26-1076), indicating the absence of long-range ordering and the presence of small crystallite domains compared with highly crystalline graphitic materials.[32,33] A weak reflection at 41.6°, which was assigned to the (100) plane, suggested the partial presence of sp^2 graphitic carbon domains within the CQD framework.[34,35] The size of the CQDs dispersed in water, which was determined *via* DLS, ranged from 4 to 13 nm, featuring an average diameter of 9.03 nm (Fig. 2B). These findings were consistent with the TEM results (Fig. 2C), which revealed the presence of uniformly dispersed spherical nanoparticles featuring sizes between 3.5 and 11 nm, confirming the nanoscale dimension and morphological uniformity of the CQDs.

Furthermore, the surface chemistry of the CQDs was investigated *via* FTIR analysis. As depicted in Fig. 3A, the characteristic absorption bands at 3016, 960, and 910 cm^{-1} are assigned to =C–H stretching and bending vibrations,[36,37] whereas the bands at 1630 and 719 cm^{-1} correspond to in-plane sp^2 C=C vibrations and out-of-plane C–H bending, respectively, confirming the presence of polyaromatic domains in the CQD framework.[38,39] Additionally, the bands at 3200, 1565, and 1340 cm^{-1} indicated the incorporation of amino groups *via* N–H stretching, N–H bending, and C–N vibrations, respectively.[40] Furthermore, the presence of surface oxygenated functionalities was evidenced by the bands at 3450 (O–H), 1717 (C=O), and 1170 cm^{-1} (C–O), which were attributable to hydroxyl, carbonyl, and carboxyl groups, respectively.[38,40] These abundant nitrogen- and oxygen-containing functional groups were expected to enhance the hydrophilicity, surface reactivity, and antimicrobial performance of the CQDs.

The elemental composition and bonding states of the CQDs were investigated *via* XPS analysis. The survey spectrum (see the SI Fig. S1A) confirmed the presence of carbon, oxygen, and nitrogen, in addition to 3.43% bromine, which corresponded to free bromide ions (Br^-), most plausibly originating from CTAB dissociation during synthesis. The high-resolution C 1s spectrum (Fig. 3B) displayed a dominant signal at 284.2 eV, corresponding to the C=C, C–C, and CH_x species of the carbon skeleton.[35] Additionally, the peaks at 285.2, 286.0, 287.6, and 288.9 eV were assigned to C–N (amino), C–O–C/C–O (ether), C=O/N=C–N (carbonyl/pyridinic N), and C=O–C (carboxyl/ester) functionalities, respectively.[41,42] The N 1s spectrum (Fig. 3C) exhibited peaks at 398.9, 400.0, 401.1, and 402.5 eV, corresponding to pyridinic N (C–N=C), pyrrolic-N (C–NH–C), graphitic N (N–C_3), and oxidized N (N–O), respectively.[43,44] Moreover, a minor peak was observed at 407 eV, which was attributed to the residual nitrate species resulting from incomplete nitric acid decomposition.[45] Furthermore, the O 1s spectrum (Fig. S1B) was deconvoluted to reveal component peaks at 531.5, 533.7, and 535.0 eV, corresponding to carbonyl, hydroxyl, and terminal carboxyl/ester groups,[46] whereas the peak at 532.6 eV was attributed to ether linkages or surface-adsorbed nitrate species.[47,48] These findings confirmed the incorporation of abundant nitrogen- and oxygen-containing functional groups (C–N=C, C–NH–C, N–C_3, N–O, C–O, C=O, O–C–O, and O–C=O) on the CQD surface, which was consistent with the FTIR results. The coexistence of hydrophilic oxygenated and nitrogenous functionalities was expected to enhance the water solubility, chemical reactivity, and pathogen-interacting capability of the CQDs, underpinning their high antimicrobial and antiviral performance.[49,50]

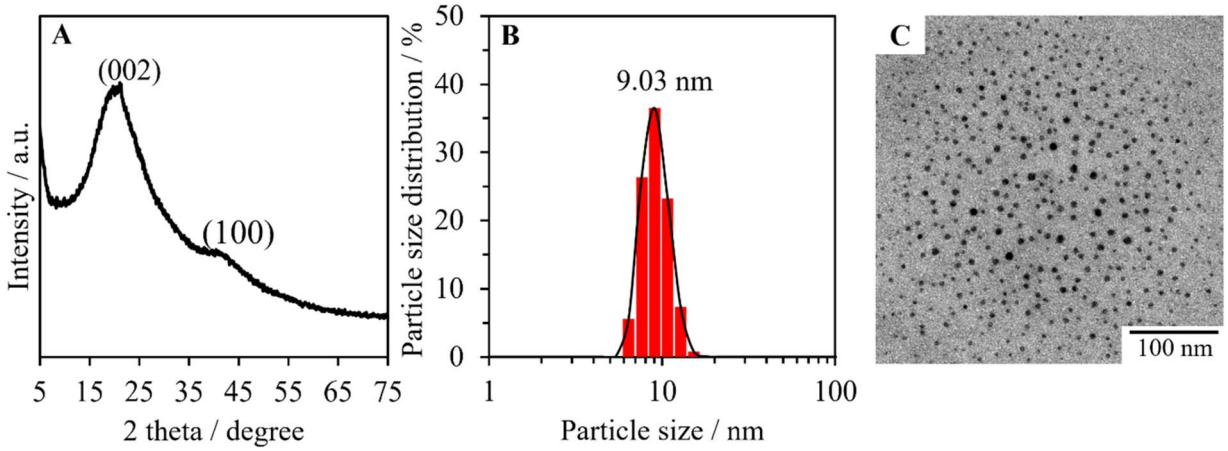

Fig. 2 (A) XRD pattern, (B) particle size distribution, and (C) TEM image of the CQDs.

3.2 Optical properties of the CQDs

The optical properties of the CQDs were investigated *via* UV-vis absorption and photoluminescence (PL) spectroscopy. The CQD aqueous solution displayed a yellow-brown color when observed under daylight, whereas it exhibited an intense blue fluorescence under UV irradiation at 365 nm (inset, Fig. 4A). The UV-vis spectrum (Fig. 4A) demonstrated a weak band at 270 nm, which was assigned to the π–π* transition of C=C bonds in the CQD core structure.[34] Additional absorption features were observed at 340 and 400 nm, corresponding to the *n*–π* transition of C=O and the π–π* transition of N=O bonds, respectively, originating from oxygen- and nitrogen-containing

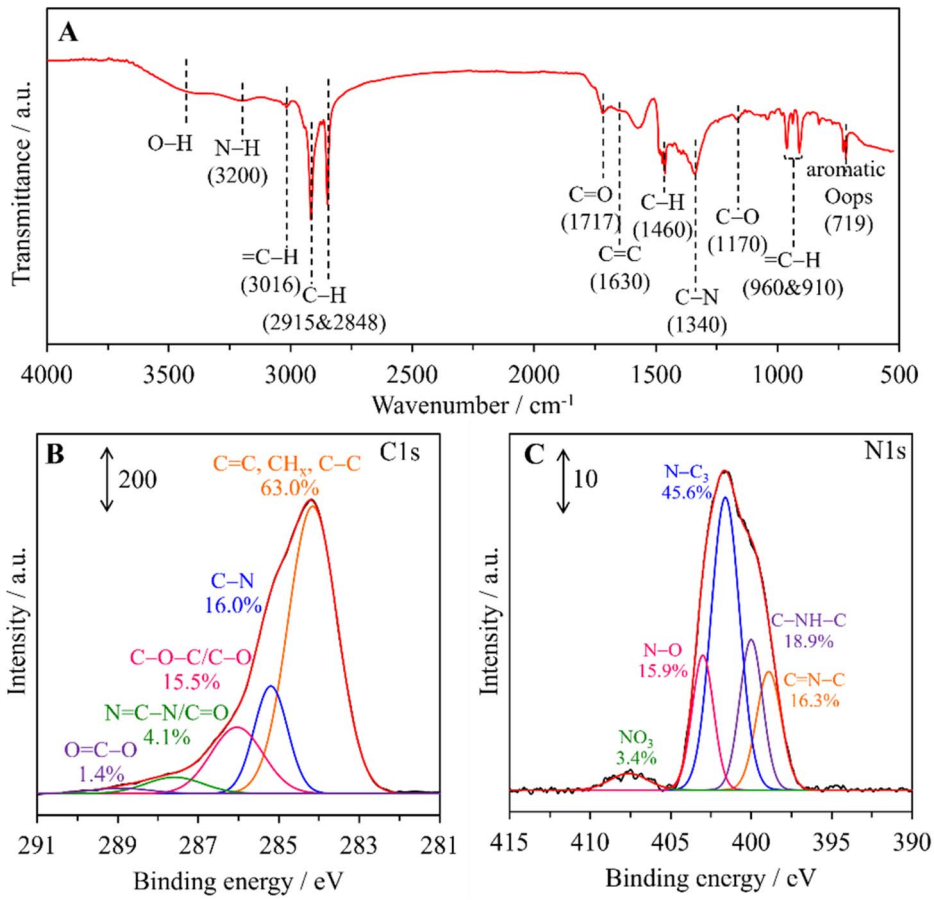

Fig. 3 (A) FTIR spectrum and (B and C) XPS spectra of the CQDs: (B) high-resolution C 1s and (C) N 1s spectra.

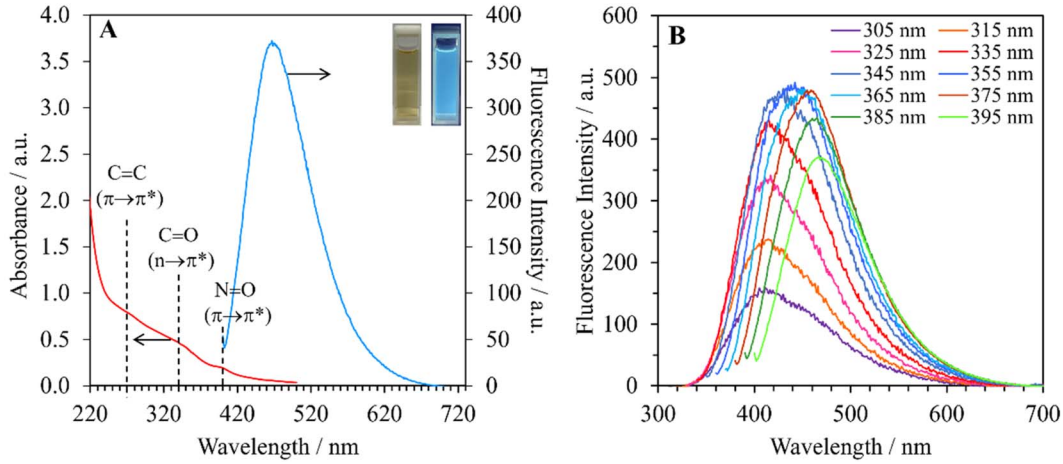

Fig. 4 (A) UV-vis absorption spectrum of the CQDs. Inset: photographs of an aqueous CQD solution under daylight and UV irradiation at 365 nm, exhibiting bright blue PL emission. (B) Fluorescence emission spectra of the CQDs recorded at different excitation wavelengths, demonstrating excitation-dependent PL behavior.

functionalities in the surface passivation layer.[35,51,52] These results were consistent with the incorporation of heteroatoms indicated *via* the XPS and FTIR analyses.

The PL spectra of the CQDs in the excitation wavelength range of 305–395 nm (Fig. 4B) exhibited a prominent excitation-dependent emission. An increase in the excitation wavelength resulted in a gradual redshift of the emission maximum, presenting a characteristic feature of CQDs due to surface defect states and heteroatom-related electronic transitions. The emission intensity steadily increased from 305 to 355 nm, reaching a maximum at ~440 nm, after which it decreased with a further redshift of the excitation wavelength to 395 nm. This behavior indicated the interplay between the surface passivation functional groups, particle size distribution, and electronic structure of the CQDs.[52]

The CQDs synthesized using NR latex displayed an intense blue PL signal, displaying tunable excitation-dependent emission, which confirmed their well-passivated surface states. These optical features, in conjunction with the abundant hydrophilic and heteroatom-containing surface functionalities, suggest that the CQDs are promising materials for antimicrobial and antiviral applications as well as for potential use in optical sensors and bioimaging platforms.

3.3 Antimicrobial and antiviral activity of the CQDs

The antibacterial activity of the CQDs was evaluated against *E. coli* (Gram-negative) and *S. aureus* (Gram-positive) bacteria using disk diffusion and broth dilution assays. Clear inhibition zones were observed for both species in the disk diffusion assay (Fig. S2), confirming the effective suppression of bacterial growth by the CQDs. As presented in Table 1, inhibition is not detected for the negative control (distilled water), whereas the positive control (95% ethanol) exhibits measurable inhibition zones, validating the reliability of the experimental design. The inhibition zone diameter recorded for *S. aureus* was larger than that measured for *E. coli*, which was consistent with the broth dilution assay results. The MIC and MBC values of the CQDs were determined as 3.75–7.50 μg mL^{-1} for *S. aureus* and 15.00 μg mL^{-1} for *E. coli* (Table 1). The higher MIC and MBC values observed for *E. coli* emphasized the lower sensitivity of Gram-negative bacteria, which could be attributed to the complex multilayer structure of their cell walls that offered limited permeability to antimicrobial agents.[53,54] Conversely, the simpler peptidoglycan-rich cell wall of Gram-positive bacteria, such as *S. aureus*, was more susceptible to nanoparticle penetration and functional group interactions.[55]

Furthermore, the time-kill assay demonstrated the rapid bactericidal action of the CQDs. Exposure to CQDs at the MBC led to a >99.9% reduction in viable *E. coli* and *S. aureus* populations within 5 min (Fig. S3). Moreover, a regrowth assay was performed to clarify the nature of the antimicrobial action of the CQDs. After CQD treatment, the bacterial suspensions were streaked onto fresh nutrient agar and incubated under standard conditions. Colony formation was not detected for any CQD-treated samples (Fig. S4 and S5), whereas normal bacterial growth was observed for the untreated controls. The absence of regrowth confirmed that the CQDs exhibited true bactericidal activity rather than exerting merely a bacteriostatic effect. This observation was fully consistent with the observed >99.9% reduction in colony-forming units, which is widely accepted as the benchmark criterion for defining bactericidal activity. These results indicated that the NR-derived CQDs exhibited potent and broad-spectrum antibacterial activity, combining both rapid killing kinetics and long-lasting inhibitory effects. The high antibacterial activity of the CQDs was consistent with the abundant nitrogen- and oxygen-containing surface functionalities, which would enhance membrane interactions (Fig. 5A and related discussion).

The antimicrobial and antiviral activities of the NR-derived CQDs were evaluated against diverse microorganisms, including Gram-positive bacteria (*S. aureus*, *M. luteus*, and *B. subtilis*), Gram-negative bacteria (*E. coli* and *K. pneumoniae*),

Table 1 Antibacterial activity of the CQDs against *E. coli* (Gram negative) and *S. aureus* (Gram-positive), as determined using disk diffusion and broth dilution assays

	Clear zone of inhibition (mm)				
Bacteria	Negative control	Positive control	CQD	MIC (μg mL^{-1})	MBC (μg mL^{-1})
E. coli	0.00 ± 0.00	1.00 ± 0.00	2.19 ± 0.26	15.0	15.0
S. aureus	0.00 ± 0.00	1.88 ± 0.23	4.81 ± 0.26	3.75	7.50

fungi (*C. albicans* and *A. niger*), and influenza A virus (H3N2; a representative viral model). As depicted in Fig. 5B, the CQDs achieve >99.9% reduction in the viability of *S. aureus*, *M. luteus*, *E. coli*, *C. albicans*, *A. niger*, and H3N2 within 5 min of exposure, emphasizing their broad-spectrum efficacy. Conversely, the CQDs exhibited lower activities against *K. pneumoniae* (95.3% reduction) and *B. subtilis* (1.5% reduction). The reduced sensitivity of *K. pneumoniae* was plausibly caused by its polysaccharide capsule, which served as a protective barrier against external agents.[56,57] *B. subtilis* displayed an even lower degree of susceptibility, which was consistent with its capacity to form highly resistant endospores. Endospores possess a multilayered protective architecture, comprising the exosporium, proteinaceous coat, cortex, and dehydrated core enriched in dipicolinic

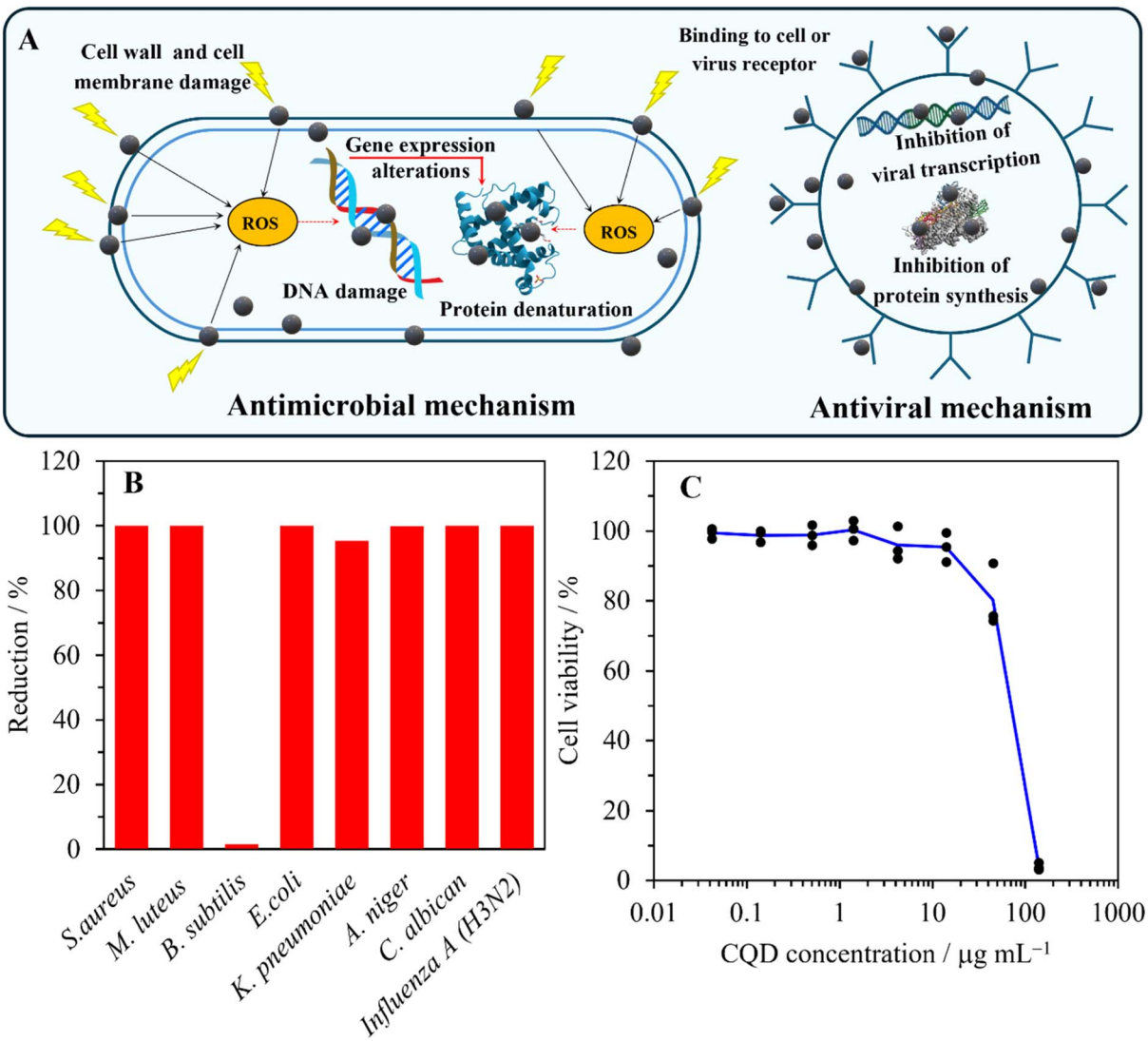

Fig. 5 (A) Schematic of the proposed mechanisms of the CQDs, exhibiting ROS-mediated cell wall/membrane damage and biomolecular disruption in bacteria (left) and the inhibition of viral attachment, replication, and budding (right). (B) Percentage reduction of selected microorganisms and influenza A virus (H3N2) after treatment with the NR-derived CQDs. (C) Cell viability of HaCaT keratinocyte cells after 24 h of exposure to different CQD concentrations, as determined using the MTT assay.

acid and small acid-soluble spore proteins. These structural features collectively provide exceptional tolerance to ROS, dehydration, and membrane-disruptive agents. Additionally, the extremely low metabolic activity of spores reduces their susceptibility to oxidative or redox-mediated antimicrobial effects, including those induced by the nitrogen-doped CQDs.[58]

These findings were consistent with the results of previous studies, which revealed that the nitrogen-doped CQDs exhibited enhanced antimicrobial activity because of the presence of protonated amino groups capable of facilitating electrostatic interactions with negatively charged microbial membranes.[59–61] As illustrated in Fig. 5A, upon binding, the CQDs induce physical membrane damage, and when exposed to light, they generate ROS, such as hydroxyl and superoxide radicals. These ROS would promote oxidative stress, leading to DNA damage, protein denaturation, and lipid peroxidation, disrupting the essential cellular functions.[62,63] Therefore, the strong antimicrobial effects observed in this study reflected the interplay between the CQD size, surface functional groups, and inherent structural defenses of the microbial species.

In addition to antibacterial and antifungal effects, the CQDs displayed potent antiviral activity against influenza A virus (H3N2). Viral infection typically proceeds *via* attachment, penetration, replication, and budding.[17] The CQDs interfered with the multiple stages of the aforementioned cycle. They prevented viral binding and penetration by interacting with cell-surface receptors, inhibited replication *via* direct interactions with viral nucleic acids or enzymes, and suppressed budding, reducing the release of new infectious particles.[64] Additionally, the as-prepared nitrogen-doped CQDs demonstrated several potential application opportunities. Their rapid microbial inactivation capability indicated their potential for application in disinfectant formulations, antimicrobial surface coatings, protective textiles, and food-packaging systems that would benefit from fast and broad-spectrum microbial suppression.

3.4 Cytotoxicity of the CQDs

The cytotoxicity of CQDs is assessed against HaCaT keratinocyte cells using the MTT assay, which is a widely accepted model for the evaluation of dermal toxicity relevant to skincare and disinfectant applications.[65] As depicted in Fig. 5C, cell viability remains above 90% after 24 h of exposure to CQDs at concentrations up to 16 μg mL^{-1}, indicating the excellent biocompatibility of the material at working doses. This minimal dermal toxicity is attributed to the high selectivity of the CQDs for bacteria, which possess a highly negative surface charge that promotes strong electrostatic binding and ROS-mediated membrane disruption. Conversely, HaCaT keratinocytes feature a thicker, more neutral, cholesterol-rich bilayer that exhibits strong antioxidant defenses, resulting in substantially weaker CQD binding and considerably lower susceptibility to damage.[66] At high concentrations of CQD solution, cell viability decreases by ~25% and ~97% at 48.8 and 140.0 μg mL^{-1}, respectively, demonstrating a clear dose-dependent effect. Importantly, the antimicrobial and antiviral efficacies of the CQDs at noncytotoxic concentrations are comparable with those of 70% ethanol, which is a standard disinfectant. Furthermore, the CQDs do not exhibit the substantial cytotoxic effects previously reported for ethanol concentrations of >20% in keratinocytes.[67] These results emphasize the potential of the NR-derived CQDs as safe, cost-effective, and skin-compatible antimicrobial agents for next-generation disinfectants or topical formulations.

3.5 Comparison of antimicrobial activity

A comparison of the antimicrobial activity of the synthesized CQDs with that of previously reported CQD systems is presented in Table S1. Oxygen-rich CQDs prepared using *Typha angustifolia*,[68] mixed fruit peels,[69] or *Syzygium cumini* L.[70] mainly rely on weak oxidative stress and limited electrostatic interactions, resulting in high MIC values (100–1000 μg mL^{-1}) and slow inactivation (24 h). Vitamin C-derived CQDs can efficiently generate ROS; however, they remain negatively charged, leading to slow cell attachment and long exposure times (24–96 h) at the dosages of 100–300 μg mL^{-1}.[25] Metal-assisted CQD systems, such as Mn-doped CQDs[71] or Cu-coupled CQDs,[72] commonly exhibit high antimicrobial potency because the incorporated metal centers facilitate redox cycling and ROS generation. However, their performance fundamentally relies on the presence of metal ions, which leads to concerns related to cytotoxicity, leaching, bioaccumulation, and long-term environmental safety. Although Cu-CQDs can achieve substantially low MIC values, their synthesis typically involves copper species and antibiotic-derived precursors, rendering them unsuitable for applications that require inherently safe, metal-free, and eco-friendly antimicrobial agents. N-doped CQDs derived from Osmanthus or aromatic precursors exhibit good charge-transfer behavior but require a concentration of ≥250–1000 μg mL^{-1} owing to limited nitrogen incorporation and slow ROS production.[73,74] Conversely, the as-developed NR-derived CQDs have the combined advantages of high nitrogen contents, rapid ROS generation, ultrasmall sizes, and strong membrane affinity induced during CTAB-assisted synthesis. These characteristics enable ultrafast and broad-spectrum activity (≤5 min) at an exceptionally low MIC of 3.75–15 μg mL^{-1}. Furthermore, the CQDs exhibit low cytotoxicity and are completely devoid of metal ions and antibiotic residues. The mechanistic advantages of strong electrostatic binding, efficient oxidative disruption, and viral-envelope interference collectively contribute to the superior performance of the NR-based CQDs compared to that of all previously reported biomass-derived CQD systems.

3.6 Physicochemical properties of hydrochar and AC

The crystalline structures of hydrochar, CAC, and TAC were examined *via* XRD (Fig. 6A). All the samples displayed broad reflections at $2\theta \approx 18–28°$ and 41–45°, corresponding to the (002) and (100) planes of graphitic carbon (JCPDS card no. 41-1487), which represented the interlayer stacking and lateral size of aromatic domains, respectively.[75,76] Compared with the CAC pattern, the TAC profile exhibited a noticeable shift in both reflections to larger diffraction angles, indicating a reduction in interlayer spacing. Furthermore, the enhanced intensity of the

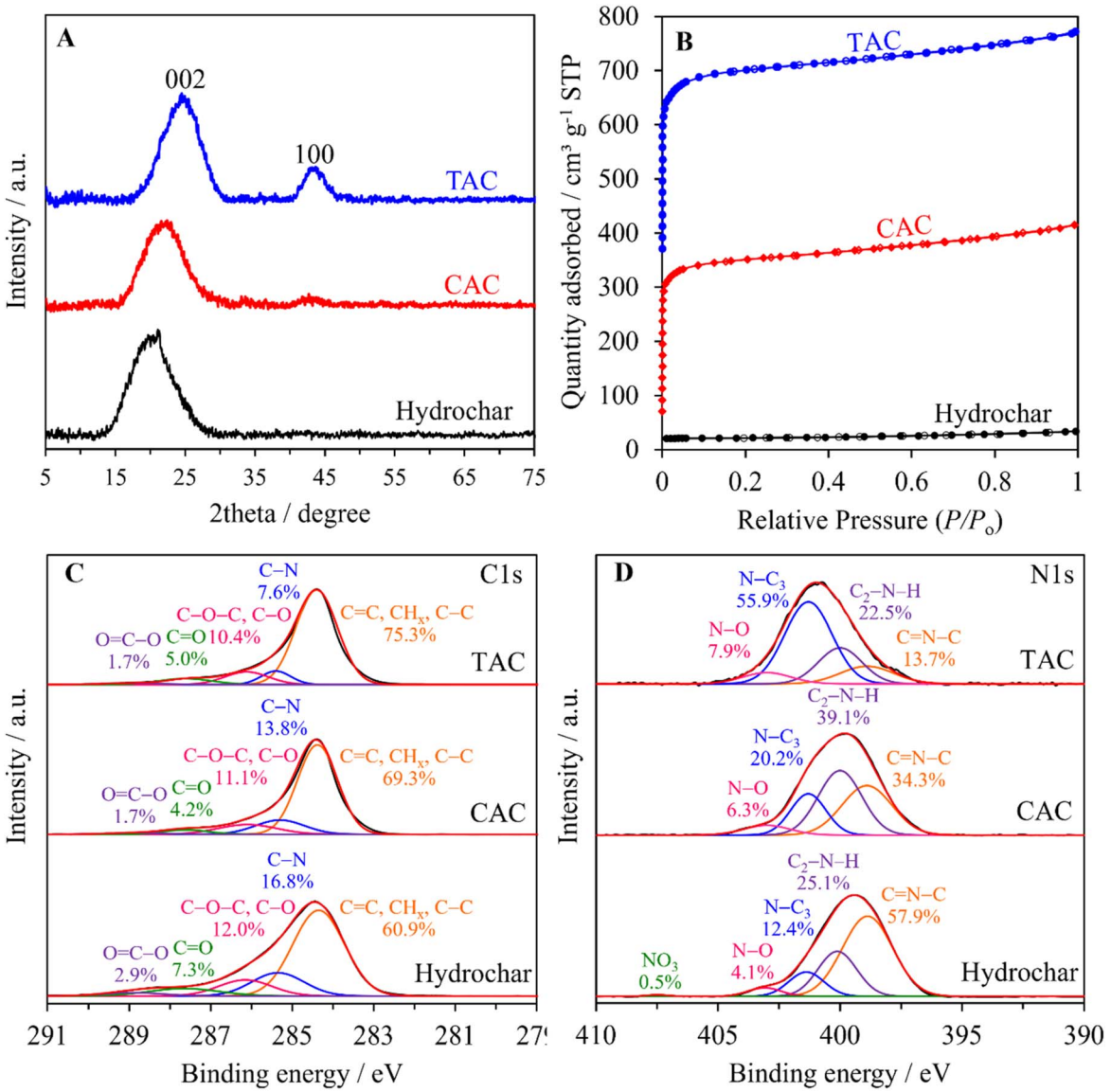

Fig. 6 (A) XRD patterns, (B) N_2 adsorption–desorption isotherms, and high-resolution XPS (C) C 1s and (D) N 1s spectra of (a) hydrochar, (b) CAC, and (c) TAC.

TAC reflections indicated higher structural ordering and the improved stacking of aromatic layers.[77] The textural properties of the materials were assessed *via* N_2 adsorption–desorption isotherms (Fig. 6B). CAC and TAC demonstrated type-I isotherms characteristic of microporous structures, whereas hydrochar exhibited negligible N_2 uptake. TAC possessed a higher adsorption volume, S_{BET}, D_p, and V_t than CAC (Table S2). This was attributed to the more substantial release of volatile matter at higher activation temperatures. The resulting S_{BET} values ranged from 994 to 1167 $m^2\ g^{-1}$ depending on the activation method, and TAC exhibited the highest porosity. These findings suggested that physical activation at higher temperatures would generate a more ordered carbon framework featuring higher porosity than chemical activation.

The elemental composition and surface chemical states of hydrochar, CAC, and TAC were examined *via* XPS. The survey spectra (Fig. S6) confirmed the presence of carbon, oxygen, and nitrogen in all the samples. The deconvoluted C 1s spectra (Fig. 6C) revealed contributions from C=C/CH_x/C–C (284.3 eV), C–N (285.3 eV), C–O (286.1 eV), C=O (287.6 eV), and O–C=O (288.9 eV),[41] indicating the presence of diverse oxygenated and nitrogenous functionalities. The N 1s spectra (Fig. 6D) displayed bands corresponding to pyridinic N (398.9 eV), pyrrolic N (400.1 eV), graphitic N (401.4 eV), and oxidized N (403.1 eV).[43–45] Furthermore, the O 1s spectra (Fig. S7) confirmed the existence of carbonyl (531.5 eV), ether/adsorbed nitrate (532.6 eV), hydroxyl (533.7 eV), and terminal carboxyl/ester (535.0 eV) species.[78,79] The surface elemental composition expressed as the

atomic concentration, as obtained *via* XPS analysis, is summarized in Table S3.

Activation considerably influenced the surface chemistry of the synthesized materials. Both CAC and TAC exhibited higher carbon contents than hydrochar, reflecting carbon enrichment during activation,[80] whereas the oxygen and nitrogen contents decreased because of the volatilization of heteroatom-containing groups at high temperatures.[81] Notably, TAC possessed a higher proportion of graphitic N than CAC, which was consistent with enhanced graphitization under high-temperature physical activation.[82–84] Conversely, CAC retained higher pyridinic and pyrrolic N contents, suggesting the better preservation of disordered carbon domains and heteroatom functionalities under chemical activation condictions.[85] These results confirmed that activation pathways strongly modulated the surface chemistry of carbon materials. Thermal activation promoted the stabilization of graphitic nitrogen species within the aromatic lattices, whereas chemical activation favors the retention of oxygen- and nitrogen-containing groups. The combination of large surface areas and abundant surface heteroatoms rendered the resulting AC materials promising for adsorption applications, where both textural properties and surface functionalities would contribute to enhanced adsorption capacity and selectivity.[86–88]

3.7 Adsorptive removal of DCF from aqueous solutions

The adsorption performance of hydrochar and AC toward DCF is depicted in Fig. 7 (left). Hydrochar exhibited the lowest DCF uptake (10.88 mg g^{-1}), which was consistent with its limited surface area and low porosity (Table S2). Conversely, CAC demonstrated the highest capacity (116.30 mg g^{-1}), outperforming TAC (101.03 mg g^{-1}) despite its smaller surface area and total pore volume. This enhancement should be attributed to the higher proportion of pyridinic and pyrrolic N species on the CAC surface (Table S3), which promoted DCF adsorption *via* electrostatic and hydrogen-bonding interactions.[89,90]

The kinetic analysis of DCF adsorption on hydrochar, CAC, and TAC was performed using various kinetic equations (Fig. S8 and Table S4), among which the pseudo-second-order model provided the best fit for all the samples, as evidenced by the highest correlation coefficients (R^2 = 0.982–0.999). Conversely, the pseudo-first-order and Ritchie models yielded lower correlation coefficients, particularly for hydrochar, confirming that the adsorption process was dominated by chemisorption rather than physical diffusion.[91] Additionally, the rate constants (k_2) of CAC and TAC were lower than the corresponding value of hydrochar, indicating slower adsorption kinetics for AC sorbents. However, CAC and TAC exhibited substantially higher equilibrium adsorption capacities (121.95 and 102.04 mg g^{-1}, respectively) than hydrochar (11.33 mg g^{-1}). This suggested that although initial adsorption on hydrochar was rapid, the limited surface area and low porosity of the material restricted the overall uptake.

As shown in Fig. 7 (right), the adsorption of DCF on AC is governed by a combination of pore structural characteristics and surface chemistry. The well-developed microporous network provides confined spaces that accommodate DCF molecules *via* micropore filling, which is a dominant pathway for pharmaceuticals with comparable molecular sizes. This is consistent with previous reports on carbonaceous adsorbents and the excellent Langmuir fit observed in this study.[92] Furthermore, interactions between the aromatic framework of AC and the conjugated rings of DCF stabilize adsorption *via* π–π electron donor–acceptor interactions, which is a widely accepted mechanism for the adsorption of aromatic pollutant on graphitic domains.[93] Surface heteroatoms generated during activation, including oxygen- and nitrogen-containing groups, provide hydrogen-bonding sites that interact with the

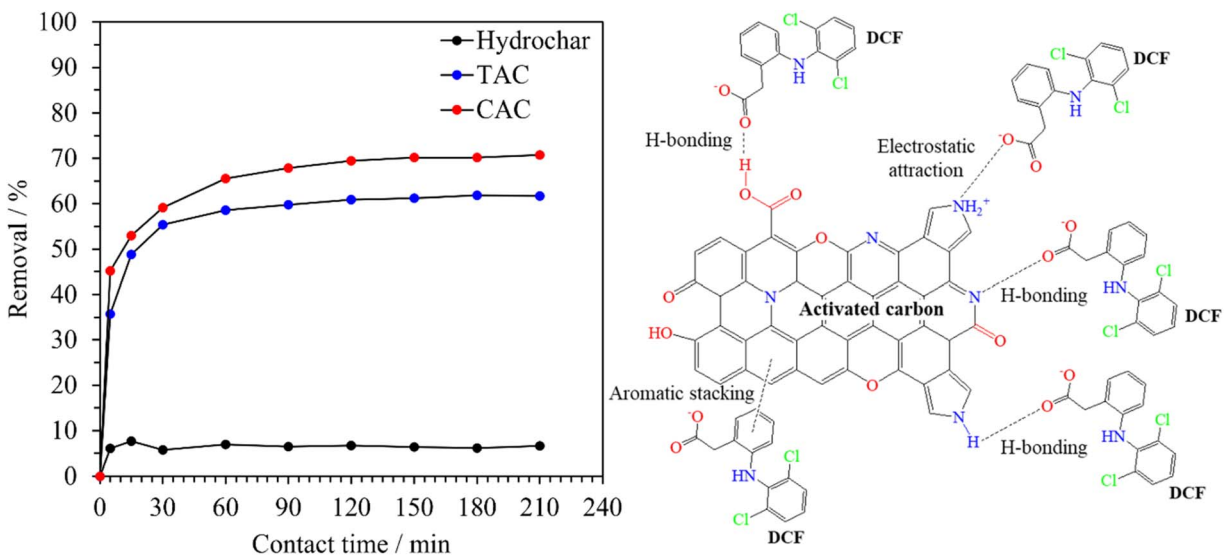

Fig. 7 (Left) Effects of the contact time on DCF adsorption by hydrochar, CAC, and TAC. (Right) Proposed interactions of diclofenac molecules with the surface functional groups of AC. (Adsorption conditions: initial DCF concentration = 50 mg L^{-1}; DCF solution volume = 150 mL; adsorbent dosage = 45 mg; pH = 6; temperature = 25 °C).

carboxylate and amide functionalities of DCF, particularly at defect-rich or edge sites.[94] Furthermore, depending on the protonation states of DCF and the carbon surface, electrostatic contributions may arise, particularly when nitrogen functionalities induce the formation of positively polarized regions. The DCF molecule, possessing a hydrophobic aromatic structure, exhibits a high affinity for the nonpolar graphitic regions, leading to partitioning within the carbon matrix.[95] Therefore, these results emphasize that DCF uptake is governed by surface chemistry, rather than the surface area alone, guiding the sustainable design of biomass-derived AC for pharmaceutical removal.

The effects of the contact time on DCF adsorption by CAC at different initial concentrations (10–50 mg L^{-1}) are depicted in Fig. 8. The removal of DCF from the aqueous solution was rapid in the first 30 min, achieving 53–81% uptake depending on the initial concentration, and gradually approached equilibrium after ~120 min. The rapid initial adsorption suggested the abundance of accessible sites on the CAC surface, whereas the slow approach to equilibrium indicated site saturation.[96] At equilibrium, removal efficiencies decreased from 95.3% at 10 mg L^{-1} to 77.0% at 50 mg L^{-1}, which indicated a finite number of active sites. The equilibrium data were fitted using Langmuir and Freundlich isotherm models (Table S5). The Langmuir model ($R^2 = 0.998$) provided slightly higher correlation coefficients than the Freundlich model ($R^2 = 0.990$), indicating that DCF adsorption on CAC occurred *via* monolayer coverage on a homogeneous surface. The maximum Langmuir capacity was 126.82 mg g^{-1}, featuring a high affinity constant ($k_L = 0.582$ L mg^{-1}). The Freundlich model yielded a heterogeneity factor (n) of 3.10, which was >1, indicating favorable adsorption. However, the relatively small Freundlich constant (k_F) suggested a minor contribution from multilayer or heterogeneous adsorption.[97] The reusability of the CAC adsorbent for the removal of DCF from water was preliminarily evaluated. After each adsorption cycle, the spent CAC adsorbent was recovered *via* filtration, thoroughly washed with ethanol, and dried at 100 °C overnight. The repeatability test results (Fig. 8B) demonstrated that although the DCF removal efficiency slightly decreased with increasing number of cycles, the adsorbent successfully retained 92% of its initial removal capacity after the fifth cycle. This high retention rate suggested good structural stability and excellent adsorption performance retention of the CAC material under the tested regeneration conditions. Collectively, these findings confirm that CAC is a reusable and economically viable adsorbent that affords a facile synthesis method, emphasizing its practical potential for the sustainable removal of pharmaceutical residues from water matrices.

4. Conclusions

This study demonstrated a sustainable co-production strategy that converted NR latex into two high-value carbon nanomaterials, including antimicrobial CQDs and AC. The hydrothermally derived CQDs exhibited intense blue fluorescence as well as broad-spectrum antibacterial, antifungal, and antiviral activities, achieving a killing efficiency of >99.9% within 5 min. Furthermore, they exhibited low cytotoxicity, emphasizing their potential as safe and effective alternatives to conventional disinfectants. Moreover, hydrochar-derived AC possessed a large surface area, well-developed microporous structures, and abundant oxygen- and nitrogen-containing functional groups, which collectively enabled rapid adsorption and high diclofenac uptake. Notably, the CAC adsorbent synthesized *via* chemical activation outperformed its counterparts and achieved a maximum diclofenac uptake capacity of 126.82 mg g^{-1}, demonstrating rapid adsorption kinetics and monolayer coverage that were consistent with the Langmuir model.

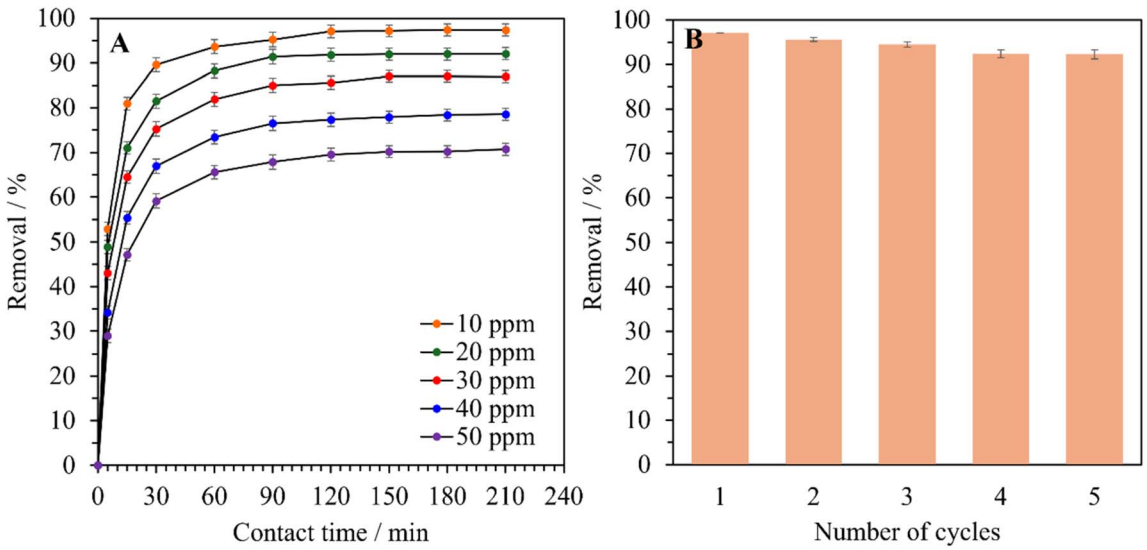

Fig. 8 (A) Effects of the contact time on DCF adsorption over CAC at different initial concentrations. (Adsorption conditions: DCF solution volume = 150 mL; adsorbent dosage = 45 mg; pH = 6; temperature = 25 °C). (B) Reusability of CAC for DCF adsorption (adsorption conditions: initial DCF concentration = 10 mg L^{-1}; DCF solution volume = 150 mL; adsorbent dosage = 45 mg; pH = 6; temperature = 25 °C).

Furthermore, the multifunctional characteristics of the two coproduced carbon materials suggest their promising potential for real-world applications. The CQDs featuring rapid and broad-spectrum antimicrobial activity are suitable materials for incorporation into disinfectant formulations, antimicrobial coatings, and biomedical or protective materials. Moreover, hydrochar-derived AC exhibits considerable potential for the adsorption-based removal of pharmaceutical pollutants, supporting its application in modular water-purification devices and advanced treatment systems designed for the elimination of emerging contaminants. These potential applications emphasize the practical relevance of the integrated strategy developed in this study.

Author contributions

Satit Yousatit: conceptualization, investigation, methodology, formal analysis, validation, writing – original draft, data curation. Sakdinun Nuntang: formal analysis, writing review and editing; Toshiyuki Yokoi: writing review and editing; Chawalit Ngamcharussrivichai: conceptualization, supervision, validation, writing review & editing; Napida Hinchiranan: conceptualization, supervision, writing review & editing.

Conflicts of interest

The authors declare that they have no known competing financial interests or personal relationships that could have appeared to influence the work reported in this paper.

Data availability

The data supporting this article have been included as part of the supplementary information (SI). Supplementary information: S1. Materials characterization in detail; S2. Antimicrobial activity assay in detail; S3. Anti-influenza A virus (H3N2) activity assay in detail; S4. Adsorption data analysis; S5. Material characterization and results; Tables S1–S5 and Fig. S1–S8. See DOI: https://doi.org/10.1039/d5ra07708g.

Acknowledgements

The authors express their gratitude for the financial and technical support from the Center of Excellence on Petrochemical and Materials Technology (PETROMAT), Chulalongkorn University (grant no. PETROMAT-PT-64-03), and from the Center of Excellence in Catalysis for Bioenergy and Renewable Chemicals (CBRC), Faculty of Science, Chulalongkorn University. S. Yousatit also acknowledges the Postdoctoral Fellowship provided by Chulalongkorn University through the Second Century Fund (C2F).

References

1 C. Ingrao, R. Strippoli, G. Lagioia and D. Huisingh, Water scarcity in agriculture: An overview of causes, impacts and approaches for reducing the risks, *Heliyon*, 2023, **9**, e18507, DOI: 10.1016/j.heliyon.2023.e18507.
2 G. Wang, S. Kumar, Z. Huang and R. Liu, Water resource management and policy evaluation in Middle Eastern countries: Achieving sustainable development goal 6, *Desalination Water Treat.*, 2024, **320**, 100829, DOI: 10.1016/j.dwt.2024.100829.
3 L. S. Fernandes, A. Galvao, R. Santos and S. Monteiro, Impact of water reuse on agricultural practices and human health, *Environ. Res.*, 2023, **216**, 114762, DOI: 10.1016/j.envres.2022.114762.
4 M. Collivignarelli, A. Abbà, I. Benigna, S. Sorlini and V. Torretta, Overview of the main disinfection processes for wastewater and drinking water treatment plants, *Sustainability*, 2017, **10**, 1704, DOI: 10.3390/su10010086.
5 R. Rienzie, L. R. Sendanayake and N. M. Adassooriya, Chapter 11 - Nanotechnology applications for removal of disinfection by-products from water, in *Disinfection By-Products in Drinking Water*, ed. M. N. V. Prasad, Butterworth-Heinemann, United Kingdom, 2020, pp. 253–277.
6 R. Xiao, Y. Deng, Z. Xu and W. Chu, Disinfection byproducts and their precursors in drinking water sources: origins, influencing factors, and environmental insights, *Engineering*, 2024, **36**, 36–50, DOI: 10.1016/j.eng.2023.08.017.
7 Z. Dong, J. Qi, L. Yue, H. Zhou, L. Chen, J. Gu, Y. He and H. Wu, Biomass-based carbon quantum dots and their agricultural applications, *Plant Stress*, 2024, **11**, 100411, DOI: 10.1016/j.stress.2024.100411.
8 A. Liu, Z. Dai, D. Ouyang, B. Mahara, L. Yang and X. Chen, In situ conversion of graphite into graphene quantum dots (GQDs) towards upcycling of spent lithium-ion batteries, *Green Chem.*, 2025, **27**, 12460–12471, DOI: 10.1039/d5gc03503a.
9 B. Luo, H. Yang, B. Zhou, S. M. Ahmed, Y. Zhang, H. Liu, X. Liu, Y. He and S. Xia, Facile synthesis of luffa sponge activated carbon fiber based carbon quantum dots with green fluorescence and their application in Cr(VI) determination, *ACS Omega*, 2020, **5**, 5540–5547, DOI: 10.1021/acsomega.0c00195.
10 E. Dhandapani, N. Duraisamy, P. Periasamy and P. V. T, Highly green fluorescent carbon quantum dots synthesis via hydrothermal method from fish scale, *Mater. Today Proc.*, 2020, **26**, A1–A5, DOI: 10.1016/j.matpr.2021.04.396.
11 H. L. Yang, L. F. Bai, Z. R. Geng, H. Chen, L. T. Xu, Y. C. Xie, D. J. Wang, H. W. Gu and X. M. Wang, Carbon quantum dots: Preparation, optical properties, and biomedical applications, *Mater. Today Adv.*, 2023, **18**, 100376, DOI: 10.1016/j.mtadv.2023.100376.
12 X. Liu, Y. Wang, Y. Gu and W. Lu, One-step hydrothermal synthesis of nitrogen-doped carbon-quantum-dots for detection and efficient removal of high-concentrations nicotine from tobacco wastewater under visible light, *Chem. Eng. J.*, 2024, **499**, 156573, DOI: 10.1016/j.cej.2024.156573.
13 G. A. Zalmi, P. Khobrekar, R. W. Jadhav, R. R. Naik, S. Sinari, S. T. Bugde and S. V. Bhosale, Hydrothermal synthesis of

tartaric acid functionalized amino acid CQD for sensing of Hg^{2+} and Fe^{3+} ions in aqueous medium, *ChemistrySelect*, 2024, **9**, e202304825, DOI: 10.1002/slct.202304825.

14 A. Majid, K. Ahmad, L. Tan, W. Niaz, W. Na, L. Huiru and J. Wang, The advanced role of carbon quantum dots in nano-food science: Applications, bibliographic analysis, safety concerns, and perspectives, *C*, 2024, **11**, 1, DOI: 10.3390/c11010001.

15 J. T. Sakdapipanich and P. Rojruthai, Natural rubber: Biosynthesis, structure, properties and application, in *Natural Rubber Materials, Volume 1: Blends and IPNs*, ed. S. Thomas, C. Han Chan, L. Pothen, J. Joy and H. Maria, The Royal Society of Chemistry, London, 2013, pp. 28–52.

16 F. Xu, D. Wu, R. Fu and B. Wei, Design and preparation of porous carbons from conjugated polymer precursors, *Mater. Today*, 2017, **20**, 629–656, DOI: 10.1016/j.mattod.2017.04.026.

17 N. H. Hussen, A. H. Hasan, Y. M. FaqiKhedr, A. Bogoyavlenskiy, A. R. Bhat and J. Jamalis, Carbon dot based carbon nanoparticles as potent antimicrobial, antiviral, and anticancer agents, *ACS Omega*, 2024, **9**, 9849–9864, DOI: 10.1021/acsomega.3c05537.

18 Q. Li, X. Shen and D. Xing, Carbon quantum dots as ROS-generator and -scavenger: A comprehensive review, *Dyes Pigm.*, 2023, **208**, 110784, DOI: 10.1016/j.dyepig.2022.110784.

19 J. Lei, K. Wang, B. Deng, Y. Li, S. Zhang and Y. Cao, Enhanced oxygen reduction of porous N-doped carbon nanosheets with graphitic N and defects obtained from coal-based graphene quantum dots, *J. Alloys Compd.*, 2022, **914**, 165359, DOI: 10.1016/j.jallcom.2022.165359.

20 P. Zhang, H. Liu, S. Wang, J. Zhang, Q. Chen, L. Fu, Z. Yin, F. Tang, X. Zuo and L. Zhang, Interfacial kinetics regulation and electrochemical optimization in ultrasonic-induced sponge cadmium nucleation, *Ultrason. Sonochem.*, 2025, **120**, 107491, DOI: 10.1016/j.ultsonch.2025.107491.

21 N. A. Travlou, D. A. Giannakoudakis, M. Algarra, A. M. Labella, E. Rodríguez-Castellón and T. J. Bandosz, S- and N-doped carbon quantum dots: Surface chemistry dependent antibacterial activity, *Carbon*, 2018, **135**, 104–111, DOI: 10.1016/j.carbon.2018.04.018.

22 J. Yang, X. Zhang, Y. H. Ma, G. Gao, X. Chen, H. R. Jia, Y. H. Li, Z. Chen and F. G. Wu, Carbon dot-based platform for simultaneous bacterial distinguishment and antibacterial applications, *ACS Appl. Mater. Interfaces*, 2016, **8**, 32170–32181, DOI: 10.1021/acsami.6b10398.

23 Q. Dou, X. Fang, S. Jiang, P. L. Chee, T.-C. Lee and X. J. Loh, Multi-functional fluorescent carbon dots with antibacterial and gene delivery properties, *RSC Adv.*, 2015, **5**, 46817–46822, DOI: 10.1039/c5ra07968c.

24 H. B. Ahmed and H. E. Emam, Environmentally exploitable biocide/fluorescent metal marker carbon quantum dots, *RSC Adv.*, 2020, **10**, 42916–42929, DOI: 10.1039/d0ra06383e.

25 H. Li, J. Huang, Y. Song, M. Zhang, H. Wang, F. Lu, H. Huang, Y. Liu, X. Dai, Z. Gu, Z. Yang, R. Zhou and Z. Kang, Degradable carbon dots with broad-spectrum antibacterial activity, *ACS Appl. Mater. Interfaces*, 2018, **10**, 26936–26946, DOI: 10.1021/acsami.8b08832.

26 Y. Xue, C. Liu, G. Andrews, J. Wang and Y. Ge, Recent advances in carbon quantum dots for virus detection, as well as inhibition and treatment of viral infection, *Nano Converg.*, 2022, **9**, 15, DOI: 10.1186/s40580-022-00307-9.

27 A. K. Priya, L. Gnanasekaran, S. Rajendran, J. Qin and Y. Vasseghian, Occurrences and removal of pharmaceutical and personal care products from aquatic systems using advanced treatment- A review, *Environ. Res.*, 2022, **204**, 112298, DOI: 10.1016/j.envres.2021.112298.

28 C. F. de Azevedo, N. F. de Souza, F. B. Cardoso, A. Fuhr, E. C. Lima, A. G. Osorio and F. Machado Machado, Experimental and modeling of potassium diclofenac uptake on activated carbon, *Environ. Sci. Pollut. Res. Int.*, 2024, **31**, 48650–48662, DOI: 10.1007/s11356-024-34407-2.

29 D. C. C. da Silva Medeiros, M. Usman, P. Chelme-Ayala and M. Gamal El-Din, Biochar-enhanced removal of naphthenic acids from oil sands process water: Influence of feedstock and chemical activation, *Energy Environ. Sustain.*, 2025, **1**, 100028, DOI: 10.1016/j.eesus.2025.100028.

30 C. Rodriguez Correa, M. Bernardo, R. P. P. L. Ribeiro, I. A. A. C. Esteves and A. Kruse, Evaluation of hydrothermal carbonization as a preliminary step for the production of functional materials from biogas digestate, *J. Anal. Appl. Pyrolysis*, 2017, **124**, 461–474, DOI: 10.1016/j.jaap.2017.02.014.

31 C. Lei, J. Yang, J. Hu and X. Sun, On the calculation of $TCID_{50}$ for quantitation of virus infectivity, *Virol. Sin.*, 2021, **36**, 141–144, DOI: 10.1007/s12250-020-00230-5.

32 J. Wang, S. Li, P. Ma, Z. Guo, Q. Ma, Q. Zhao, Y. Guo, J. Zhao and G. Guan, Carbon quantum dots/Cu_2O S-scheme heterojunction for enhanced photocatalytic degradation of tetracycline, *Colloids Surf., A*, 2024, **690**, 133779, DOI: 10.1016/j.colsurfa.2024.133779.

33 J. Luo, Y. Lei, Q. Ge, M. Liu, N. Jiang, Y. H. Huang, H. Cong and J. L. Zhao, Carbon quantum dots from hemicucur[6]bit and the application for the detection of Pb^{2+}, *Spectrochim. Acta, Part A*, 2024, **317**, 124459, DOI: 10.1016/j.saa.2024.124459.

34 S. Safranko, A. Stankovic, S. Hajra, H. J. Kim, I. Strelec, M. Dutour-Sikiric, I. Weber, M. H. Bosnar, P. Grbcic, S. K. Pavelic, A. Szechenyi, Y. K. Mishra, I. Jerkovic and S. Jokic, Preparation of multifunctional N-Doped carbon quantum dots from citrus clementina peel: investigating targeted pharmacological activities and the potential application for Fe^{3+} sensing, *Pharmaceuticals*, 2021, **14**, 857, DOI: 10.3390/ph14090857.

35 R. Qiang, S. Yang, K. Hou and J. Wang, Synthesis of carbon quantum dots with green luminescence from potato starch, *New J. Chem.*, 2019, **43**, 10826–10833, DOI: 10.1039/c9nj02291k.

36 A. Madhi, B. Shirkavand Hadavand and A. H. Madhi, Environmentally friendly g-C_3N_4/carbon quantum dots nanocomposites as fluorescent and anti-spoofing inks, *Fullerenes, Nanotub. Carbon Nanostruct.*, 2023, **31**, 953–960, DOI: 10.1080/1536383x.2023.2226272.

37 J. Wang, Y. Wang, X. Li, Y. Weng, X. Dong and X. Zhao, Comparison on the effectiveness of Fourier transform infrared (FT-IR) and attenuated total reflection Fourier transform infrared (ATR-FT-IR) in characterizing plastics biodegradation by insect larvae, *Sci. Total Environ.*, 2022, **839**, 156289, DOI: 10.1016/j.scitotenv.2022.156289.

38 J. Plé, C. S. Stan, D. Zanghi, C. Genevois, S. Hajjar-Garreau and L. Balan, Photoinduced polymer-confined CQDs for efficient photoluminescent 2D/3D printing applications, *Mater. Adv.*, 2023, **4**, 5140–5148, DOI: 10.1039/d3ma00293d.

39 M. Saikia, T. Das and B. K. Saikia, A novel rapid synthesis of highly stable silver nanoparticle/carbon quantum dot nanocomposites derived from low-grade coal feedstock, *New J. Chem.*, 2022, **46**, 309–321, DOI: 10.1039/d1nj04039a.

40 A. Aygun, I. Cobas, R. N. E. Tiri and F. Sen, Hydrothermal synthesis of B, S, and N-doped carbon quantum dots for colorimetric sensing of heavy metal ions, *RSC Adv.*, 2024, **14**, 10814–10825, DOI: 10.1039/d4ra00397g.

41 S. Yousatit, H. Pitayachinchot, A. Wijitrat, S. Chaowamalee, S. Nuntang, S. Soontaranon, S. Rugmai, T. Yokoi and C. Ngamcharussrivichai, Natural rubber as a renewable carbon source for mesoporous carbon/silica nanocomposites, *Sci. Rep.*, 2020, **10**, 12977, DOI: 10.1038/s41598-020-69963-3.

42 J. Ci, Y. Tian, S. Kuga, Z. Niu, M. Wu and Y. Huang, One-pot green synthesis of nitrogen-doped carbon quantum dots for cell nucleus labeling and copper(II) detection, *Chem. – Asian J.*, 2017, **12**, 2916–2921, DOI: 10.1002/asia.201700880.

43 S. D. Dsouza, M. Buerkle, P. Brunet, C. Maddi, D. B. Padmanaban, A. Morelli, A. F. Payam, P. Maguire, D. Mariotti and V. Svrcek, The importance of surface states in N-doped carbon quantum dots, *Carbon*, 2021, **183**, 1–11, DOI: 10.1016/j.carbon.2021.06.088.

44 Ç. Kırbıyık, A. Toprak, C. Başlak, M. Kuş and M. Ersöz, Nitrogen-doped CQDs to enhance the power conversion efficiency of perovskite solar cells via surface passivation, *J. Alloys Compd.*, 2020, **832**, 154897, DOI: 10.1016/j.jallcom.2020.154897.

45 D. Sebastián, M. Nieto-Monge, S. Pérez-Rodríguez, E. Pastor and M. Lázaro, Nitrogen doped ordered mesoporous carbon as support of PtRu nanoparticles for methanol electro-oxidation, *Energies*, 2018, **11**, 831, DOI: 10.3390/en11040831.

46 X. Zhu, M. Li, X. F. Zhang, J. Liu and J. Yao, Mxene functionalized wood composite films for efficient electromagnetic interference shielding and pressure sensing, *Adv. Mater. Technol.*, 2023, **9**, 2301009, DOI: 10.1002/admt.202301009.

47 J. V. Rojas, M. Toro-Gonzalez, M. C. Molina-Higgins and C. E. Castano, Facile radiolytic synthesis of ruthenium nanoparticles on graphene oxide and carbon nanotubes, *Mater. Sci. Eng. B*, 2016, **205**, 28–35, DOI: 10.1016/j.mseb.2015.12.005.

48 X. He, B. Liu, S. Zhang, H. Li, J. Liu, Z. Sun and H. Chang, Nickel nitrate hydroxide holey nanosheets for efficient oxygen evolution electrocatalysis in alkaline condition, *Electrocatalysis*, 2021, **13**, 37–46, DOI: 10.1007/s12678-021-00686-3.

49 S. Bhatt, R. Pathak, V. D. Punetha and M. Punetha, Recent advances and mechanism of antimicrobial efficacy of graphene-based materials: a review, *J. Mater. Sci.*, 2023, **58**, 7839–7867, DOI: 10.1007/s10853-023-08534-z.

50 M. Y. Xia, Y. Xie, C. H. Yu, G. Y. Chen, Y. H. Li, T. Zhang and Q. Peng, Graphene-based nanomaterials: the promising active agents for antibiotics-independent antibacterial applications, *J. Contr. Release*, 2019, **307**, 16–31, DOI: 10.1016/j.jconrel.2019.06.011.

51 F. Wu, H. Su, K. Wang, W. K. Wong and X. Zhu, Facile synthesis of N-rich carbon quantum dots from porphyrins as efficient probes for bioimaging and biosensing in living cells, *Int. J. Nanomedicine*, 2017, **12**, 7375–7391, DOI: 10.2147/IJN.S147165.

52 P. Siahcheshm and P. Heiden, High quantum yield carbon quantum dots as selective fluorescent turn-off probes for dual detection of Fe^{2+}/Fe^{3+} ions, *J. Photochem. Photobiol., A*, 2023, **435**, 114284, DOI: 10.1016/j.jphotochem.2022.114284.

53 S. P. Denyer and J. Y. Maillard, Cellular impermeability and uptake of biocides and antibiotics in Gram-negative bacteria, *J. Appl. Microbiol.*, 2002, **92**, 35S–45S, DOI: 10.1046/j.1365-2672.92.5s1.19.x.

54 M. Godoy-Gallardo, U. Eckhard, L. M. Delgado, Y. J. D. de Roo Puente, M. Hoyos-Nogues, F. J. Gil and R. A. Perez, Antibacterial approaches in tissue engineering using metal ions and nanoparticles: From mechanisms to applications, *Bioact. Mater.*, 2021, **6**, 4470–4490, DOI: 10.1016/j.bioactmat.2021.04.033.

55 Y. N. Slavin, J. Asnis, U. O. Hafeli and H. Bach, Metal nanoparticles: understanding the mechanisms behind antibacterial activity, *J. Nanobiotechnology*, 2017, **15**, 65, DOI: 10.1186/s12951-017-0308-z.

56 R. Ramakrishnan, A. V. Nair, K. Parmar, R. S. Rajmani, D. Chakravortty and D. Das, Combating biofilm-associated Klebsiella pneumoniae infections using a bovine microbial enzyme, *npj Biofilms Microbiomes*, 2024, **10**, 119, DOI: 10.1038/s41522-024-00593-7.

57 X. Liu, Q. Xu, X. Yang, H. Heng, C. Yang, G. Yang, M. Peng, E. C. Chan and S. Chen, Capsular polysaccharide enables Klebsiella pneumoniae to evade phagocytosis by blocking host-bacteria interactions, *mBio*, 2025, **16**, e0383824, DOI: 10.1128/mbio.03838-24.

58 A. Romero-Rodriguez, B. Ruiz-Villafan, C. F. Martinez-de la Pena and S. Sanchez, Targeting the impossible: A review of new strategies against endospores, *Antibiotics*, 2023, **12**, 248, DOI: 10.3390/antibiotics12020248.

59 S. Pandiyan, L. Arumugam, S. P. Srirengan, R. Pitchan, P. Sevugan, K. Kannan, G. Pitchan, T. A. Hegde and V. Gandhirajan, Biocompatible carbon quantum dots derived from sugarcane industrial wastes for effective nonlinear optical behavior and antimicrobial activity applications, *ACS Omega*, 2020, **5**, 30363–30372, DOI: 10.1021/acsomega.0c03290.

60 C. Zhao, X. Wang, L. Yu, L. Wu, X. Hao, Q. Liu, L. Lin, Z. Huang, Z. Ruan, S. Weng, A. Liu and X. Lin, Quaternized carbon quantum dots with broad-spectrum antibacterial activity for the treatment of wounds infected

with mixed bacteria, *Acta Biomater.*, 2022, **138**, 528–544, DOI: 10.1016/j.actbio.2021.11.010.

61 H. Wang, Q. Wang, Q. Wang, W. Dong, Y. Liu, Q. Hu, X. Song, S. Shuang, C. Dong and X. Gong, Metal-free nitrogen-doped carbon nanodots as an artificial nanozyme for enhanced antibacterial activity, *J. Clean. Prod.*, 2023, **411**, 137337, DOI: 10.1016/j.jclepro.2023.137337.

62 D. I. Abu Rabe, M. M. Al Awak, F. Yang, P. A. Okonjo, X. Dong, L. R. Teisl, P. Wang, Y. Tang, N. Pan, Y. P. Sun and L. Yang, The dominant role of surface functionalization in carbon dots' photo-activated antibacterial activity, *Int. J. Nanomedicine*, 2019, **14**, 2655–2665, DOI: 10.2147/IJN.S200493.

63 X. Dong, W. Liang, M. J. Meziani, Y. P. Sun and L. Yang, Carbon dots as potent antimicrobial agents, *Theranostics*, 2020, **10**, 671–686, DOI: 10.7150/thno.39863.

64 P. Innocenzi, D. De Forni and F. Lori, Antiviral activity of carbon dots: Strategies and mechanisms of action, *Small Struct.*, 2024, **6**, 2400401, DOI: 10.1002/sstr.202400401.

65 I. Colombo, E. Sangiovanni, R. Maggio, C. Mattozzi, S. Zava, Y. Corbett, M. Fumagalli, C. Carlino, P. A. Corsetto, D. Scaccabarozzi, S. Calvieri, A. Gismondi, D. Taramelli and M. Dell'Agli, HaCaT cells as a reliable in vitro differentiation model to dissect the inflammatory/repair response of human keratinocytes, *Mediators Inflammation*, 2017, **2017**, 7435621, DOI: 10.1155/2017/7435621.

66 A. S. Klein, M. Schaefer, T. Korte, A. Herrmann and A. Tannert, HaCaT keratinocytes exhibit a cholesterol and plasma membrane viscosity gradient during directed migration, *Exp. Cell Res.*, 2012, **318**, 809–818, DOI: 10.1016/j.yexcr.2012.02.007.

67 J. M. Calderon-Montano, J. J. Jimenez-Alonso, E. Guillen-Mancina, E. Burgos-Moron and M. Lopez-Lazaro, A 30-s exposure to ethanol 20% is cytotoxic to human keratinocytes: possible mechanistic link between alcohol-containing mouthwashes and oral cancer, *Clin. Oral Invest.*, 2018, **22**, 2943–2946, DOI: 10.1007/s00784-018-2602-z.

68 P. Nallasamy, P. Kannan, M. Selvaraj, M. A. Assiri and S. Natarajan, Natural biomass-derived carbon quantum dots: a path to antioxidant, anticancer, antibiofilm, and bacterial bioimaging potential, *Mikrochim. Acta*, 2025, **192**, 286, DOI: 10.1007/s00604-025-07132-x.

69 Q. Yu, M. Zhang, A. S. Mujumdar and M. Huang, Evaluation of antioxidant, antimicrobial and bacterial labeling capacities of four plant byproduct carbon dots, *Food Biosci.*, 2023, **56**, 103091, DOI: 10.1016/j.fbio.2023.103091.

70 R. B. Pricilla, M. Maruthapandi, A. Durairaj, I. Kuritka, J. H. T. Luong and A. Gedanken, Biomass-derived Carbon dots and their coated surface as a potential antimicrobial agent, *Biomass Convers. Biorefin.*, 2023, **14**, 17705–17716, DOI: 10.1007/s13399-023-03968-6.

71 M. Tariq, S. Shivalkar, H. Hasan, A. K. Sahoo and M. P. Sk, Manganese Doping in Biomass Derived Carbon Dots Amplifies White Light-Induced Antibacterial Activity, *ACS Omega*, 2023, **8**, 49460–49466, DOI: 10.1021/acsomega.3c08586.

72 H. Miao, P. Wang, Y. Cong, W. Dong and L. Li, Preparation of Ciprofloxacin-Based Carbon Dots with High Antibacterial Activity, *Int. J. Mol. Sci.*, 2023, **24**, 6814, DOI: 10.3390/ijms24076814.

73 Y. Ma, M. Zhang, H. Wang, B. Wang, H. Huang, Y. Liu and Z. Kang, N-doped carbon dots derived from leaves with low toxicity via damaging cytomembrane for broad-spectrum antibacterial activity, *Mater. Today Commun.*, 2020, **24**, 101222, DOI: 10.1016/j.mtcomm.2020.101222.

74 H. Wang, F. Lu, C. Ma, Y. Ma, M. Zhang, B. Wang, Y. Zhang, Y. Liu, H. Huang and Z. Kang, Carbon dots with positive surface charge from tartaric acid and m-aminophenol for selective killing of Gram-positive bacteria, *J. Mater. Chem. B*, 2021, **9**, 125–130, DOI: 10.1039/d0tb02332a.

75 J. Serafin, B. Dziejarski and J. Sreńscek-Nazzal, An innovative and environmentally friendly bioorganic synthesis of activated carbon based on olive stones and its potential application for CO_2 capture, *Sustain. Mater. Technol.*, 2023, **38**, e00717, DOI: 10.1016/j.susmat.2023.e00717.

76 Z.-G. Yang, N.-N. Liu, S. Dong, F.-S. Tian, Y.-P. Gao and Z.-Q. Hou, Supercapacitors based on free-standing reduced graphene oxides/carbon nanotubes hybrid films, *SN Appl. Sci.*, 2018, **1**, 47, DOI: 10.1007/s42452-018-0059-y.

77 T. Qiu, J. G. Yang, X. J. Bai and Y. L. Wang, The preparation of synthetic graphite materials with hierarchical pores from lignite by one-step impregnation and their characterization as dye absorbents, *RSC Adv.*, 2019, **9**, 12737–12746, DOI: 10.1039/c9ra00343f.

78 A. Ganguly, S. Sharma, P. Papakonstantinou and J. Hamilton, Probing the Thermal Deoxygenation of Graphene Oxide Using High-Resolution In Situ X-ray-Based Spectroscopies, *J. Phys. Chem. C*, 2011, **115**, 17009–17019, DOI: 10.1021/jp203741y.

79 M. Park, J. Ryu, Y. Kim and J. Cho, Corn protein-derived nitrogen-doped carbon materials with oxygen-rich functional groups: a highly efficient electrocatalyst for all-vanadium redox flow batteries, *Energy Environ. Sci.*, 2014, **7**, 3727–3735, DOI: 10.1039/c4ee02123a.

80 G. Bonassa, L. T. Schneider, V. B. Canever, P. A. Cremonez, E. P. Frigo, J. Dieter and J. G. Teleken, Scenarios and prospects of solid biofuel use in Brazil, *Renew. Sustain. Energy Rev.*, 2018, **82**, 2365–2378, DOI: 10.1016/j.rser.2017.08.075.

81 W. Dilokekunakul, P. Teerachawanwong, N. Klomkliang, S. Supasitmongkol and S. Chaemchuen, Effects of nitrogen and oxygen functional groups and pore width of activated carbon on carbon dioxide capture: Temperature dependence, *Chem. Eng. J.*, 2020, **389**, 124413, DOI: 10.1016/j.cej.2020.124413.

82 J. Zhao, Y. Liu, X. Quan, S. Chen, H. Yu and H. Zhao, Nitrogen-doped carbon with a high degree of graphitization derived from biomass as high-performance electrocatalyst for oxygen reduction reaction, *Appl. Surf. Sci.*, 2017, **396**, 986–993, DOI: 10.1016/j.apsusc.2016.11.073.

83 A. Kumar, A. Ganguly and P. Papakonstantinou, Thermal stability study of nitrogen functionalities in a graphene

network, *J. Phys. Condens. Matter*, 2012, **24**, 235503, DOI: 10.1088/0953-8984/24/23/235503.

84 Y. F. Lu, S. T. Lo, J. C. Lin, W. Zhang, J. Y. Lu, F. H. Liu, C. M. Tseng, Y. H. Lee, C. T. Liang and L. J. Li, Nitrogen-doped graphene sheets grown by chemical vapor deposition: synthesis and influence of nitrogen impurities on carrier transport, *ACS Nano*, 2013, **7**, 6522–6532, DOI: 10.1021/nn402102y.

85 C. Rahmatunnisa, R. I. Chaerun, C. S. Budi and N. S. Gultom, Transforming chitosan into N-doped carbon for efficient CO_2 capture: A comprehensive review, *Appl. Surf. Sci. Adv.*, 2025, **27**, 100774, DOI: 10.1016/j.apsadv.2025.100774.

86 S. He, Q. Chen, G. Chen, G. Shi, C. Ruan, M. Feng, Y. Ma, X. Jin, X. Liu, C. Du, C. He, H. Dai and C. Cao, N-doped activated carbon for high-efficiency ofloxacin adsorption, *Microporous Mesoporous Mater.*, 2022, **335**, 111848, DOI: 10.1016/j.micromeso.2022.111848.

87 B. Chu, Y. Lou, Y. Tan, J. Lin and X. Liu, Nitrogen-doped mesoporous activated carbon from Lentinus edodes residue: an optimized adsorbent for pharmaceuticals in aqueous solutions, *Front. Chem.*, 2024, **12**, 1419287, DOI: 10.3389/fchem.2024.1419287.

88 Y. Maneewong, S. Chaemchuen, F. Verpoort and N. Klomkliang, Paracetamol removal from water using N-doped activated carbon derived from coconut shell: Kinetics, equilibrium, cost analysis, heat contributions, and molecular-level insight, *Chem. Eng. Res. Des.*, 2022, **185**, 163–175, DOI: 10.1016/j.cherd.2022.07.007.

89 I. Ahmed, T. Panja, N. A. Khan, M. Sarker, J. S. Yu and S. H. Jhung, Nitrogen-Doped Porous Carbons from Ionic Liquids@MOF: Remarkable Adsorbents for Both Aqueous and Nonaqueous Media, *ACS Appl. Mater. Interfaces*, 2017, **9**, 10276–10285, DOI: 10.1021/acsami.7b00859.

90 A. Bumajdad, M. J. H. Khan and J. P. Lukaszewicz, Nitrogen-enriched activated carbon derived from plant biomasses: a review on reaction mechanism and applications in wastewater treatment, *Front. Mater.*, 2023, **10**, 1218028, DOI: 10.3389/fmats.2023.1218028.

91 K. Ozcan, S. Aydin, S. Emik, A. Öngen and G. W. Kajjumba, Modelling of adsorption kinetic processes—Errors, theory and application, in, *Advanced Sorption Process Applications*, ed. S. Edebali, IntechOpen, Rijeka, 2018, DOI: 10.5772/intechopen.80495.

92 A. S. Mestre, E. Tyszko, M. A. Andrade, M. Galhetas, C. Freire and A. P. Carvalho, Sustainable activated carbons prepared from a sucrose-derived hydrochar: remarkable adsorbents for pharmaceutical compounds, *RSC Adv.*, 2015, **5**, 19696–19707, DOI: 10.1039/c4ra14495c.

93 A. A. Bayode, S. S. Emmanuel, H. Badamasi, S. O. Sanni, O. T. Ore, A. O. Dada, O. P. Ilo and A. A. Adesibikan, Efficient removal of selected neonicotinoids from single and combined systems using CuO/rGO modified musa parasidiaca biochar: insight into cost analysis, *RSC Adv.*, 2025, **15**, 34833–34845, DOI: 10.1039/d5ra03907j.

94 B. Kocabıyık, O. Üner and Ü. Geçgel, Diclofenac sodium adsorption in aqueous media by activated carbon obtained from einkorn (Triticum monococcum L.) husk, *Adsorption*, 2024, **30**, 1033–1046, DOI: 10.1007/s10450-024-00479-2.

95 N. Mao, L. Huang and Q. Shuai, Facile Synthesis of Porous Carbon for the Removal of Diclofenac Sodium from Water, *ACS Omega*, 2019, **4**, 15051–15060, DOI: 10.1021/acsomega.9b01838.

96 B. N. Bhadra, P. W. Seo and S. H. Jhung, Adsorption of diclofenac sodium from water using oxidized activated carbon, *Chem. Eng. J.*, 2016, **301**, 27–34, DOI: 10.1016/j.cej.2016.04.143.

97 T. Avcu, O. Üner and Ü. Geçgel, Adsorptive removal of diclofenac sodium from aqueous solution onto sycamore ball activated carbon – isotherms, kinetics, and thermodynamic study, *Surf. Interfaces*, 2021, **24**, 101097, DOI: 10.1016/j.surfin.2021.101097.